PAPER

Check for updates

The role of ultra-thin MnOx co-catalysts on the photoelectrochemical properties of BiVO4 photoanodes†

Rowshanak Irani, Paul Plate, Christian Höhn, Peter Bogdanoff, Markus Wollgarten, [ID] Katja Höflich, Roel van de Krol [ID] and Fatwa F. Abdi [ID] *

Metal oxide semiconductors are promising as photoanodes for solar water splitting, but they typically suffer from poor charge transfer properties due to the slow surface reaction kinetics for oxygen evolution. To overcome this, their surfaces are usually modified by depositing earth-abundant, efficient, and inexpensive water oxidation co-catalysts. While this effort has been successful in enhancing the photoelectrochemical performance, a true understanding of the nature of the improvement is still under discussion. This is due to the fact that the co-catalyst can have multiple functionalities, *e.g.*, accelerating charge transfer, passivating surface states, or modifying band bending. Disentangling these factors is challenging, but necessary to obtain a full understanding of the enhancement mechanism and better design the semiconductor/co-catalyst interface. In this study, we investigate the role of atomic layer deposited (ALD) MnOx co-catalysts and their thickness in the photoelectrochemical performance of BiVO4 photoanodes. Modified MnOx/BiVO4 samples with an optimum thickness of ∼4 nm show higher photocurrent (a factor of >3) as well as lower onset potential (by ∼100 mV) compared to the bare BiVO4. We combine spectroscopic and photoelectrochemical measurements to unravel the different roles of MnOx and explain the photocurrent trend as a function of the thickness of MnOx. X-ray photoelectron spectroscopy (XPS) studies reveal that the surface band bending of BiVO4 is modified after the addition of MnOx, therefore reducing surface recombination. At the same time, increasing the thickness of MnOx beyond the optimal 4 nm provides shunting pathways, as shown by energy dispersive X-ray scanning transmission electron microscopy (EDX-STEM) and redox electrochemistry. This cancels out the band bending effect, which explains the observed photocurrent trend. Therewith, this study provides additional insights into the understanding of the charge transfer processes occurring at the semiconductor–catalyst interface.

Introduction

Photoelectrochemical (PEC) water splitting is an attractive method to harvest solar energy and store it in the form of chemical bonds (*i.e.*, H2 and O2).[1-3] Among the two half-reactions, oxygen evolution is typically the limiting one due to the more kinetically demanding nature of the reaction.[4] Therefore, significant efforts have been dedicated to the development of efficient photoanodes to drive this reaction. Metal oxides are widely used as photoanode materials due to their low costs, general stability and scalable preparation techniques. However, their performance is often limited by poor surface charge transfer properties due to low catalytic activity and/or high surface recombination.[5-8] To overcome this, various co-catalysts, *e.g.*, RuO2, Ni/FeOOH, NiFeOx, CoPi, MnOx, *etc.* have been applied in order to modify the surface of metal oxide semiconductors,[9-16] which resulted in an improvement of the photocurrent.[14,17-25] Indeed, most metal oxide photoanodes showing high photocurrent (>5 mA cm−2) are decorated with additional co-catalysts.[16,26,27]

One of the key parameters in the optimization of a semiconductor/co-catalyst interface is the thickness of the co-catalyst. Various reports have shown that there exists an optimal thickness at which the photocurrent of the semiconductor/co-catalyst photoanode is maximized.[28,29] This behavior has been attributed to a few factors, *e.g.*, trade-off between higher catalytic activity and parasitic absorption or resistivity in thicker co-catalysts, but no clear evidence was provided up to now. In addition, despite the improvement observed with co-catalyst deposition on metal oxide photoanodes, the true role of the co-catalysts is still under debate. Already, in 2012, Gamelin pointed out conflicting proposed

Institute for Solar Fuels, Helmholtz-Zentrum Berlin für Materialien und Energie GmbH, Hahn-Meitner-Platz 1, Berlin 14109, Germany. E-mail: fatwa.abdi@helmholtz-berlin.de

† Electronic supplementary information (ESI) available. See DOI: 10.1039/d0ta00939c

5508 | *J. Mater. Chem. A*, 2020, **8**, 5508–5516

This journal is © The Royal Society of Chemistry 2020

mechanisms for photocurrent enhancement in CoPi/hematite photoanode systems.[30] More recently, differing mechanisms were also reported for CoPi/BiVO$_4$ photoanode systems. Photoinduced absorption spectroscopy (PIA)[31] and intensity modulated photocurrent spectroscopy (IMPS)[32] studies concluded that CoPi passivates surface states on BiVO$_4$, but dual working-electrode voltammetry measurements showed that CoPi also has a true catalytic role on BiVO$_4$.[33] The considerations above, therefore, clearly illustrate that we still need additional well-designed studies in order to fully unravel the role of co-catalysts on semiconductor photoanodes for water oxidation. In this work, we investigate the role of ultra-thin MnO$_x$ co-catalysts on spray-deposited BiVO$_4$ photoanodes. Spray-deposited BiVO$_4$ is among the best performing non-nanostructured BiVO$_4$ photoelectrodes,[23,34–36] and the scalability of the process has been demonstrated.[37] Earth-abundant and inexpensive MnO$_x$ has been shown to demonstrate a particularly promising behavior and low overpotential when deposited on BiVO$_4$.[38,39] Here, by using atomic layer deposition (ALD), we carefully control the thickness of the MnO$_x$ co-catalysts and examine the PEC properties of the resulting MnO$_x$/BiVO$_4$ photoanodes. The photocurrent is maximized when the thickness of MnO$_x$ is 4 nm. By examining the interface properties between MnO$_x$ and BiVO$_4$ using a combination of spectroscopy, (photo)electrochemical and microscopy techniques, we are able to show that increasing the thickness of MnO$_x$ results in decreasing surface recombination due to higher band bending, but also in the creation of shunting pathways due to direct contact between the MnO$_x$ and the conducting substrates (FTO) at pinholes. These two competing effects, therefore, result in a trade-off, which fully explains the observed photocurrent trend.

Experimental

Deposition of BiVO$_4$ thin film photoanodes

BiVO$_4$ thin films were deposited using spray pyrolysis.[23,40–42] Commercial FTO-coated glass slides (fluorine-doped tin dioxide, 15 Ω $\square^{-1}$, TEC-15, Pilkington) were used as the substrates. Prior to the deposition, a three-step cleaning procedure of ultrasonication in 10 vol% Triton™ X-100 solution (Sigma Aldrich), acetone, and ethanol, each for 15 minutes, was followed. A thin interfacial layer of SnO$_2$ was first deposited as a hole blocking layer[43] on the FTO substrates using 5 mL solution of 0.1 M SnCl$_4$ (98%, Aldrich) in ethyl acetate (99.8%, VWR Chemical). The solution was sprayed onto the substrates using a Quickmist air atomizing spray nozzle (1/4QMJAU-NC + SUQR-200). The distance between the spray nozzle and the substrate, which was placed on a hot plate, was 20 cm. To ensure adequate solvent evaporation a pulsed spray mode was used; 5 s of spraying was followed by a 53 s delay. The BiVO$_4$ precursor solution was prepared by dissolving 4 mmol Bi(NO$_3$)$_3$·5H$_2$O (98%, Alfa Aesar) in acetic acid (99.8%, Sigma Aldrich), while 4 mmol VO(AcAc)$_2$ (99%, Acros Organics) was dissolved separately in absolute ethanol (VWR Chemicals). Each solution was ultrasonicated for 15 minutes, then mixed, and finally ultrasonicated again for 15 minutes. The ratio of the acetic acid and absolute ethanol was 1 : 9 in the final 100 mL solution. The hot plate temperature was kept constant at 425 °C for the SnO$_2$ deposition and then increased to 450 °C for the BiVO$_4$ deposition. In order to improve the crystallinity, following the deposition, all samples were annealed in air at 460 °C for 2 hours.

Deposition of MnO$_x$ co-catalysts

Manganese oxide (MnO$_x$) thin films were deposited using a home-built, hot-wall atomic layer deposition (ALD) reactor.[44] The ALD reactor was constantly pumped by using a turbo molecular pump, backed-up with a roughing pump. The BiVO$_4$ substrates were mounted on a sample carrier, which is directly placed on the substrate heater in the ALD reactor. Bis(cyclopentadienyl)manganese ((EtCp$_2$)Mn, Strem Chemicals, 98%), kept at 85 °C was used as the Mn precursor, and water (Millipore, 18.2 MΩ) as the oxygen source. The reactor wall was heated to 125 °C, while the substrate temperature was kept at 150 °C. The Mn precursor and the water dosing steps were performed each for 1.5 s. After each of these dosing steps, a pump/purge/pump step was carried out, consisting of 30 s pumping/0.1 s Ar dose/30 s pumping. This led to a growth per cycle (GPC) of 1.3 Å. The film thicknesses were determined by *ex situ* spectroscopic ellipsometry (J.A. Woollam Co. spectroscopic ellipsometer, M-2000D, 193–1000 nm) on a silicon reference sample placed next to the BiVO$_4$ substrates during the deposition. The dielectric function of the MnO$_x$ film was modeled with a Tauc–Lorentz dispersion equation.[45]

Materials characterization

X-ray diffraction (XRD) measurements were done using a Bruker D8 diffractometer with Cu Kα radiation at 40 kV and 40 mA. UV-Vis spectra were measured using a PerkinElmer Lambda 950 spectrophotometer equipped with an integrating sphere. The films were placed inside the integrating sphere with a center mount sample holder (positioned at $\sim$7.5° offset from the incident light) to measure transflectance (TR), which is the sum of transmittance (T) and reflectance (R). Scanning helium ion microscopy (HIM) images were obtained with a Zeiss Orion Nanofab equipped with a secondary electron detector. HIM allows for high-resolution imaging of weakly or non-conductive nanosized features requiring a large depth of focus. The He gas pressure was set to 2 $\times$ 10^{-6} Torr for an acceleration voltage of 30 kV, probe currents ranging from 0.1 to 0.3 pA and a high spot control number to minimize the beam divergence. Monochromatic Al Kα radiation ($h\nu$ = 1486.74 eV, SPECS FOCUS 500 monochromator) was used for X-ray photoelectron spectroscopy (XPS, SPECS PHOIBOS 100 analyzer) measurements. The pass energy was set to 30 and 10 eV with step sizes of 0.5 and 0.05 eV for the survey and fine spectra, respectively. The peaks were fitted in XPSPEAK software, using Voigt profiles and a Shirley background subtraction. All spectra were calibrated with respect to the adventitious carbon C 1s peak at 284.5 eV. Samples for observation in the cross section were prepared by using a Zeiss Crossbeam 340 focused ion beam system. Elemental distribution maps were obtained using a Zeiss LIBRA 200 FE transmission electron microscope operated at 200 kV

This journal is © The Royal Society of Chemistry 2020

J. Mater. Chem. A, 2020, 8, 5508–5516 | 5509

accelerating voltage in scanning mode using a Thermo Fisher energy dispersive X-ray (EDX) spectrometer. The data shown here represent the net count signal after spectral deconvolution with an averaging kernel of 3×3 pixels.

Photoelectrochemical characterization

A three-electrode configuration using a custom Teflon cell (sample area = 0.283 cm^2) was applied for photo-electrochemical measurements.[46] The photoelectrochemical experiments were performed in a 0.1 M potassium phosphate buffer (KPi, pH $\sim$ 7) electrolyte. The buffer solution was prepared by mixing 4.625 g of potassium phosphate monobasic (KH$_2$PO$_4$, 99.5%, Merck) and 15.05 g of potassium hydrogen phosphate trihydrate (K$_2$HPO$_4$·3H$_2$O, 99%, Merck) in 1 L of Milli-Q water (18.2 MΩ cm). A Solartron SI 1286 potentiostat was used to control the potential of the working electrode. The reference electrode was an Ag/AgCl electrode (XR300, saturated KCl solution, Radiometer Analytical) and the counter electrode was a Pt wire. A blue 455 nm LED (Thorlabs M455L3, 20 mW cm^{-2}) was used as the light source. Potential conversion into the reversible hydrogen electrode (RHE) scale with respect to the Ag/AgCl potential was calculated using the Nernst equation:

$$V_{\text{RHE}} = V_{\text{Ag/AgCl}} + 0.0591 \times \text{pH} + V^0_{\text{Ag/AgCl}} \tag{1}$$

where $V^0_{\text{Ag/AgCl}}$ is 0.199 V (the standard potential of the Ag/AgCl reference electrode at 25 °C). Additional dark electrochemical measurements were performed in a 50 mM ferri/ferrocyanide electrolyte solution (potassium ferricyanide(III) (K$_3$Fe(CN)$_6$, 99%, Merck) and potassium ferrocyanide trihydrate (K$_4$-Fe(CN)$_6$·3H$_2$O, 99%, Merck)) with 0.1 M supporting potassium chloride (KCl, 99.5%, Merck).

Electrochemical mass spectrometry (EMS) was used for the detection of O$_2$ evolution. The measurements were carried out in a PEC cell with $\sim$200 μm electrolyte layers between the BiVO$_4$/MnO$_x$ photoanode and a gas-permeable membrane (ethylene–tetrafluoroethylene copolymer, Scimat), which serves as an inlet system to the differential pumped mass spectrometer system. A variable leak valve connected the first vacuum chamber to the second high-vacuum chamber, which housed the quadrupole mass spectrometer (Pfeiffer Vacuum, QMG 220 M1). Gaseous or volatile compounds formed by the photoanode were collected through the permeable membrane and detected using the mass spectrometer. Ag/AgCl was used as the reference electrode and Pt wire as the counter electrode. To calibrate the PEC cell, measurements were done with a Pt sheet as the working electrode, which is assumed to have a faradaic efficiency of 100% for the oxygen evolution reaction. A Newport solar simulator was used as the illumination source. The light power was adjusted using a calibrated spectrometer (USB2000, Ocean Optics) to 650 mW cm^{-2} for light wavelengths between 400 and 900 nm.

Intensity modulated photocurrent spectroscopy (IMPS) measurements were performed in an applied bias range of 0.6 to 1.6 V$_{\text{RHE}}$ and in a frequency range of 100 mHz to 100 kHz. A frequency response analyzer (FRA, Solartron 1250, Schlumberger) connected to an LED driver (Thorlabs DC2100) was used

in order to sinusoidally modulate the light intensity of the same blue LED source (455 nm, Thorlabs M455L3). The rms amplitude was 2 mW cm^{-2}, which was superimposed on a 20 mW cm^{-2} DC background intensity. A beam splitter was used to split the light into two beams directing towards the PEC cell and a high-speed Si photodiode (Thorlabs PDA10A-EC). The current monitor output of the as-mentioned potentiostat and the voltage signal of the high-speed Si photodiode were connected to the two channels of the FRA. The real and imaginary components of the opto-electrical gain of the sample obtained by dividing the measured photocurrent density (j_{photo}) through the voltage of the Si photodiode were obtained using the FRA. The absolute (dimensionless) complex gain of the photoelectrode was converted by multiplying with a conversion factor (0.015 V cm^2 mA^{-1}), which was determined by measuring the absolute light intensity using a calibrated photodiode (PD300UV + Ophir Nova II) and the voltage of the high-speed Si photodiode. The IMPS theory and measurement are explained in detail elsewhere.[47] Analysis steps, as described in the literature,[32,47] were applied in order to extract the charge transfer (k_{tr}) and surface recombination (k_{rec}) rate constants. From these two values, the charge transfer efficiency (η_{CT}), which can be described as the fraction of the holes that arrive at the surface and are injected into the electrolyte, was calculated using the following equation:

$$\eta_{\text{CT}} = \frac{k_{\text{tr}}}{k_{\text{tr}} + k_{\text{rec}}} \tag{2}$$

Electrochemical impedance spectroscopy (EIS) measurements were conducted under the same blue LED illumination between 0.6 and 1.6 V$_{\text{RHE}}$. The frequency was swept from 100 kHz to 100 mHz with a modulation amplitude of 10 mV.

Results and discussion

The X-ray diffractograms of the BiVO$_4$ samples with MnO$_x$ co-catalysts (2 and 6 nm) are shown in Fig. 1a. All peaks can be assigned to the BiVO$_4$ film (monoclinic, PDF 00-014-0688) and the FTO substrate. No change in the XRD patterns was observed for thicker MnO$_x$ films (up to 10 nm) on BiVO$_4$, which suggests that the MnO$_x$ co-catalyst layers are amorphous. However, some degree of crystallinity may be present, since the XRD pattern of a 20 nm MnO$_x$ film on quartz shows one small peak belonging to the MnO crystal structure (PDF 01-075-1090) (Fig. S1a, ESI†). Deposition of MnO$_x$ on BiVO$_4$ films also results in a slight increase of the absorption at wavelengths lower than $\sim$700 nm, as shown in Fig. 1b. This increase can be assigned to the additional absorption in the MnO$_x$ layers, as shown by the systematic increase of the absorptance of MnO$_x$ films on quartz with increasing thickness (Fig. S1b, ESI†). Also, the presence of different oxidation states of manganese in the MnO$_x$ layer is studied by XPS and is shown in Fig. S2.† Mn^{2+}, Mn^{3+}, and Mn^{4+} are present in all of the samples with similar values regardless of the thickness. The average oxidation state of manganese in our films is 2.7 and does not depend on the thickness of the MnO$_x$ layer.
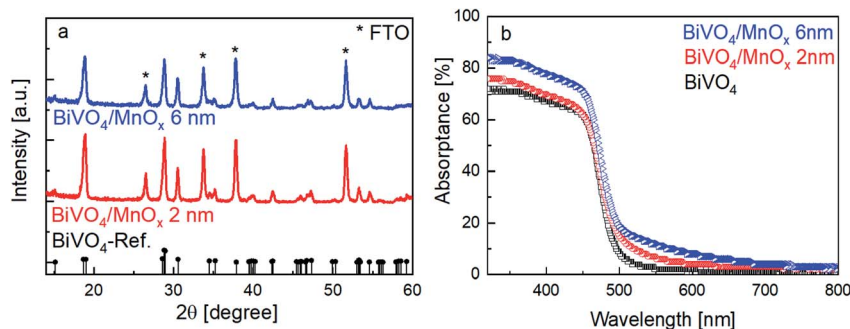
5510 | *J. Mater. Chem. A*, 2020, **8**, 5508–5516

This journal is © The Royal Society of Chemistry 2020

Fig. 1 (a) X-ray diffractograms of the $BiVO_4/MnO_x$ samples with 2 and 6 nm MnO_x thickness. In both cases, only peaks belonging to monoclinic $BiVO_4$ (black reference pattern) and FTO substrate are detected. (b) Absorptance of bare $BiVO_4$ and $BiVO_4/MnO_x$ samples with 2 and 6 nm MnO_x thickness.

Fig. 2a shows the current–voltage curves of $BiVO_4$ with different thicknesses of MnO_x co-catalysts under 455 nm LED illumination. Up to a MnO_x thickness of 4 nm, the photocurrent of the $BiVO_4$ samples at 1 V_{RHE} increases by a factor of ~3. This photocurrent increase is not due to changes in specific surface area, since the electrochemically active surface area of the $BiVO_4/MnO_x$ (4 nm) sample is actually ~25% smaller than that of the bare $BiVO_4$ (Fig. S3†). A small ~100 mV cathodic shift of the onset potential of $BiVO_4$ can also be observed. Beyond this thickness (*i.e.*, >4 nm), the photocurrent, however, starts to decrease. We confirm the reproducibility of this trend by measuring the photocurrent of at least four samples that were deposited with the same parameters but made in different spray pyrolysis and ALD batches. The production of oxygen from our films was confirmed by performing electrochemical mass spectrometry (EMS) measurements, as shown in Fig. S4†, for the $BiVO_4/MnO_x$ (4 nm) sample. With a calculated faradaic efficiency of 94 ± 1% at 0.7 V_{RHE}, almost all photocurrent is due to oxygen evolution. A comparison of the photocurrent of these samples with various thicknesses of MnO_x co-catalysts at 1 V_{RHE} is shown in Fig. 2b (black curve); the same photocurrent trend as described earlier for the other batch of samples is

maintained, which confirms the reproducibility of our samples. To reveal the underlying reason behind the observed trend, we performed intensity modulated photocurrent spectroscopy (IMPS) measurements and determined the charge transfer efficiency (η_{CT}). The complex IMPS plot at an applied potential of 1 V_{RHE} was evaluated for bare $BiVO_4$ and different thicknesses of MnO_x co-catalysts (2, 4, and 6 nm) deposited on $BiVO_4$ films (Fig. S5, ESI†). The resulting charge transfer efficiency, η_{CT}, for the bare $BiVO_4$ thin films and after addition of MnO_x co-catalysts with different thicknesses is plotted in Fig. 2b (red circles); a correlation between η_{CT} and the photocurrent is clearly present. The obtained charge transfer and surface recombination rate constants (k_{tr} and k_{rec}, respectively) are shown in Fig. S6, ESI.† While k_{tr} remains more or less constant with varying thicknesses of the MnO_x co-catalyst, k_{rec} is minimized at the same optimal thickness of 4 nm. This suggests that the main role of MnO_x on $BiVO_4$ is to suppress the surface recombination.

The photocurrent trend described above cannot be simply explained by the dark electrocatalytic activity trend of the MnO_x catalyst. Fig. S7, ESI† shows the current–voltage curves of MnO_x films with different thicknesses. The plot shows that increasing
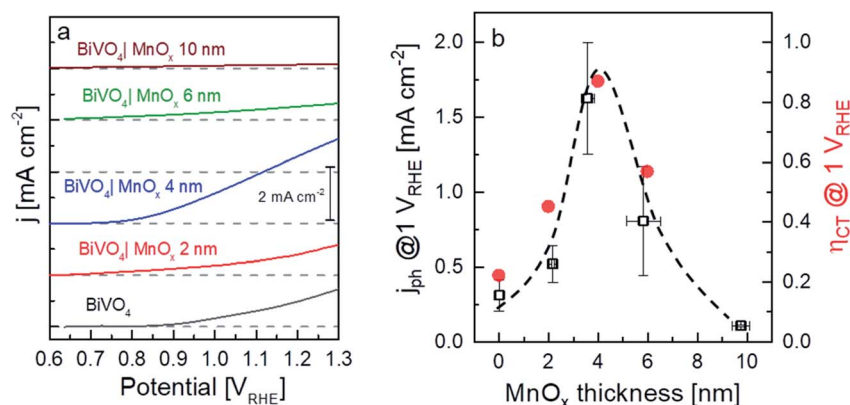

Fig. 2 (a) Linear sweep voltammetry (LSV) results of the $BiVO_4$ samples with various thicknesses of MnO_x. (b) Current (black squares, average of at least 4 measurements with different sets of samples) and charge transfer efficiency (red circles, calculated from IMPS data) of the $BiVO_4$ samples at 1 V_{RHE} with various thicknesses of MnO_x. In all cases, the light source was a 455 nm LED with 20 mW cm^{-2} power density. The dashed line is added as a guide to the eye.

This journal is © The Royal Society of Chemistry 2020

J. Mater. Chem. A, 2020, **8**, 5508–5516 | **5511**

the thickness resulted in a monotonous decrease of the current densities. It is therefore clear that MnO_x possesses a different role other than improving the catalytic activity when deposited as a co-catalyst on $BiVO_4$. This typical response was also reported by Strandwitz et al.;[39] they attributed this to the ohmic loss within the MnO_x layers.

In order to elucidate the influence of the MnO_x layer on the surface recombination of $BiVO_4$, the chemical nature of the films (and interface) was investigated by XPS. The spectra of the Bi 4f and V 2p core levels are shown in Fig. 3a and b, respectively. With increasing the thickness of the MnO_x co-catalyst, it can be clearly seen that the peaks shift towards lower binding energies. In contrast, Fig. 3c shows that the peak position of the Mn 2p core level does not shift with the increasing MnO_x thickness. The peak shifts for all these core levels are summarized in Fig. 3d.

The above-mentioned observation can be explained by the increase of band bending upon the addition of the MnO_x co-catalyst. As illustrated in Scheme 1, with increasing band bending in the $BiVO_4$ film, X-ray excitation with the same photon energy (i.e., 1486.74 eV from our Al Kα radiation) will result in detected photoelectrons with increasing kinetic energy. This translates to a shift of the core level peaks to lower binding energies, which is indeed observed in our experimental results. To further confirm this explanation, we calculated the extent of band bending in our $BiVO_4$ films, assuming the core

level peak position values of the $BiVO_4$ single crystal as those of the bulk (159.3 eV for Bi $4f_{7/2}$ and 516.9 eV for V $2p_{3/2}$).[48] The values for $BiVO_4$ films with various MnO_x thicknesses are listed in Table S1;† the values calculated using the Bi $4f_{7/2}$ peak position agree very well with those calculated using V $2p_{3/2}$. Indeed, the extent of band bending increases with the increasing film thickness.

The additional band bending explains the improvement of the PEC performance (Fig. 2a) with the increasing thickness of MnO_x (up to 4 nm). The increase of band bending has two implications: (i) increase of the space charge width; and (ii) lower surface recombination. The space charge region width can be calculated from eqn (3).

$$W = \sqrt{\frac{2\varepsilon_0\varepsilon_r}{eN_D}\left(\phi_{SC} + \Delta E - \frac{kT}{e}\right)} \qquad (3)$$

ε_0 is the vacuum permittivity and ε_r is the dielectric constant, e is the elementary charge, N_D is the donor density, ϕ_{SC} is the potential drop across the space charge layer for bare $BiVO_4$, ΔE is the shift of the core-level peak position (represents the additional potential drop with the presence of MnO_x), k is the Boltzmann constant, and T is the temperature. Increasing the thickness of the co-catalyst results in an increase of the space charge region width from 47 to 63 nm. However, assuming that all carriers generated in the space charge can be collected (Gärtner model),[49] such an increase of W only corresponds to
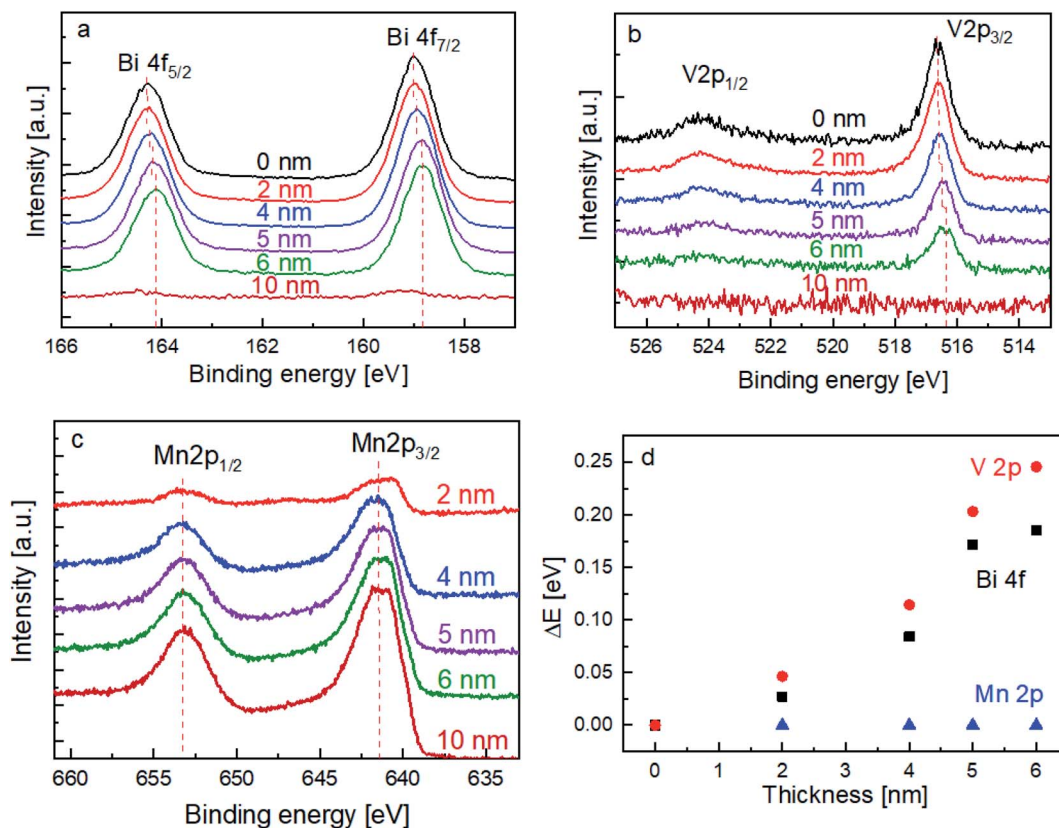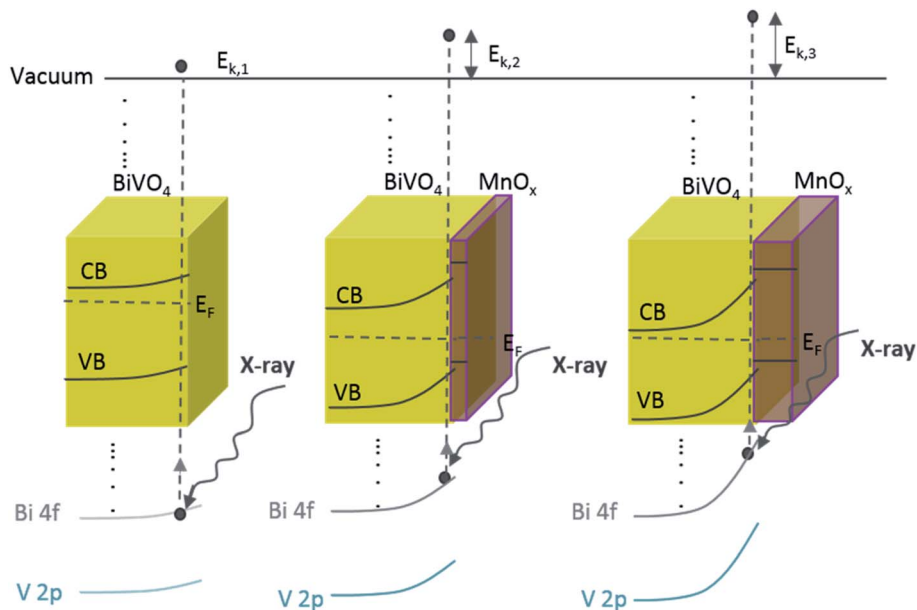

Fig. 3 Core level spectra of (a) Bi 4f, (b) V 2p, and (c) Mn 2p for bare $BiVO_4$ and $BiVO_4$ coated with different thicknesses of MnO_x (2, 4, 5, 6, and 10 nm). (d) Shift in binding energies (ΔE) for the core levels of Bi 4f, V 2p, and Mn 2p vs. various thicknesses of MnO_x.

5512 | J. Mater. Chem. A, 2020, **8**, 5508–5516

This journal is © The Royal Society of Chemistry 2020

Scheme 1 Schematic illustration of the band diagram of $BiVO_4$ and $BiVO_4$ with the increasing MnO_x thickness. Since the energy of the X-ray is constant, increasing the band bending at the interface results in photo-emitted electrons with a larger kinetic energy ($E_{k,1} < E_{k,2} < E_{k,3}$). This translates to a shift in the binding energy towards lower values, which explains our observed XPS results (Fig. 3).

~13% increase of the photocurrent generated in the space charge region. This is much smaller than the three-fold increase of the observed photocurrent (Fig. 2b), suggesting that the extension of the space charge width is a minor factor influencing the photoelectrochemical performance.

Alternatively, larger band bending may also result in a lower surface majority carrier concentration (n_{surf}) as shown in the following equation:

$$\frac{n_{surf1}}{n_{surf2}} = \exp\left(\frac{\Delta E}{kT}\right) \quad (4)$$

Since surface recombination is a function of n_{surf}, the overall surface recombination is decreased with decreasing n_{surf} and the photocurrent is improved. Based on the ~0.1 eV additional band bending observed for the optimum 4 nm $MnO_x/BiVO_4$ sample (see Fig. 3d), we estimate that n_{surf} is lowered by a factor

of ~40, which is in good agreement with the observed k_{rec} decrease from IMPS (Fig. S6, ESI†).

We note that the photocurrent enhancement can also be a result of the surface passivating effect of the MnO_x layer, which would also decrease surface recombination. Such an effect has been reported for other overlayers, such as amorphous TiO_2, Al_2O_3 and CoPi.[32,50–52] However, while we cannot completely rule out this explanation, the good quantitative agreement between the decrease of k_{rec} and n_{surf} in our films suggests that surface passivation does not play a major role.

Although the above-mentioned band bending observation can satisfactorily explain the increase of the photocurrent of $BiVO_4$ after deposition of MnO_x films, it cannot account for the overall photocurrent trend; the band bending continues to increase with the increasing MnO_x thickness, yet the photocurrent decreases when the MnO_x films are thicker than 4 nm. A competing mechanism therefore exists, which compensates for
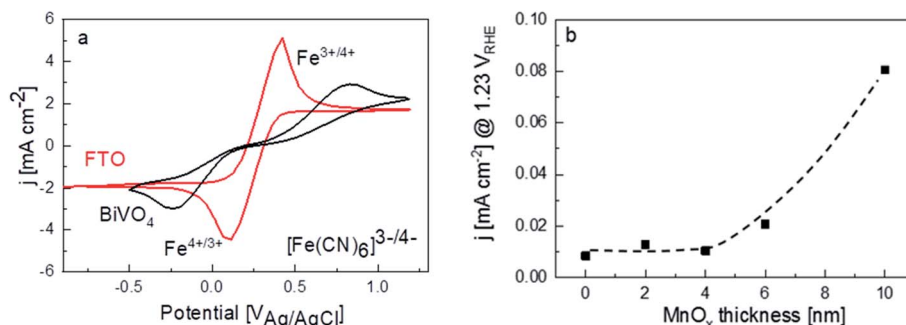

Fig. 4 (a) Voltammograms of FTO and bare $BiVO_4$ in 0.1 M KCl and 50 mM $(Fe(CN)_6)^{3-/4-}$ at the 10 mV s^{-1} scan rate. (b) Dark current measurements in 0.1 M KPi for bare $BiVO_4$ films and 2, 4, 6, and 10 nm MnO_x coated $BiVO_4$. The dashed line is added as a guide to the eye.
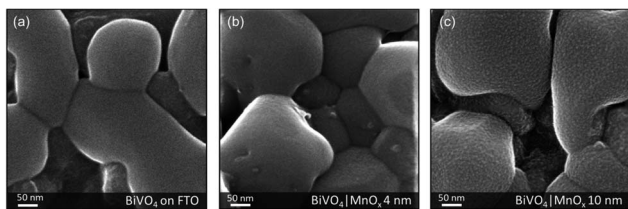
Fig. 5 Helium ion microscopy (HIM) image of (a) $BiVO_4$ on FTO, (b) $BiVO_4$ decorated with 4 nm MnO_x, and (c) $BiVO_4$ decorated with 10 nm MnO_x.

the increasing band bending at the $BiVO_4/MnO_x$ interface. One possibility is simply the lower (dark) electrochemical activity of MnO_x with the increasing thicknesses (Fig. S7, ESI†), which has been shown to be related to the poor conductivity of the MnO_x layer.[39] To confirm if this is also the case when MnO_x is deposited on $BiVO_4$, electrochemical impedance spectroscopy (EIS) was conducted for $BiVO_4$ samples with different thicknesses of MnO_x. We focus on two thicknesses of the MnO_x layer on $BiVO_4$: 4 nm as the optimum thickness and 6 nm as the thickness at which a decrease in photocurrent already occurs. The Nyquist plot for the $BiVO_4$ coated with 4 nm of MnO_x is shown in Fig. S8a.† Two semicircles can be clearly observed. We apply a resistance-based analysis method on the resistances in the films, as recently established by Moehl *et al.* for multilayer water splitting photocathodes.[53] In order to assign the identity of each semicircle, the measurements were also conducted at different applied potentials. As shown in Fig. S8a,† increasing the potential does not change the first semicircle, but a systematic decrease of the radius of the second semicircle can be observed. We therefore, attributed the first semicircle to the resistance of the MnO_x layer (R_{MnO_x}) and the second semicircle to the charge transfer resistance (R_{ct}). Fig. S8b† shows the Nyquist plot of the $BiVO_4$ films with 4 and 6 nm of MnO_x measured at ~1.23 V_{RHE}. R_{ct} decreases with the increasing MnO_x thickness, while R_{MnO_x} remains relatively constant (62.3 ± 9.3 *vs.* 64 ± 14 Ω for the 4 and 6 nm MnO_x films, respectively). These results therefore cannot explain the decrease of photocurrent for $BiVO_4$ with MnO_x films thicker than 4 nm.

Another plausible explanation for the decrease of photocurrent beyond 4 nm thickness of MnO_x is the presence of shunting pathways. For example, Boettcher and co-workers

showed that in the case of $NiFeO_x$ co-catalysts on a hematite photoanode, direct contact between $NiFeO_x$ and the underlying FTO substrate—due to the porosity or the existence of pinholes in the hematite photoanode—provides a pathway for electron–hole recombination (*i.e.*, shunting).[13] To determine whether this may be the case for our films, dark cyclic voltammetry measurements were performed for FTO and bare $BiVO_4$ in 50 mM ferri/ferrocyanide with 0.1 M supporting KCl electrolyte (Fig. 4a). The dark current for the FTO shows clear peaks corresponding to the oxidation and reduction of the $[Fe(CN)_6]^{3-}/[Fe(CN)_6]^{4}$ redox couple. For a dense $BiVO_4$ film (*i.e.*, no pinholes and the FTO is therefore not exposed to the electrolyte), these redox peaks should not be visible and only negligible dark currents are measured.[13] However, the same dark cyclic voltammetry measurements on our $BiVO_4$ film show the $[Fe(CN)_6]^{3-}/[Fe(CN)_6]^{4}$ redox peaks, albeit being smaller and shifted to higher/lower potentials. This suggests that pinholes are indeed present on our spray-pyrolysed $BiVO_4$. For the $MnO_x/BiVO_4$ samples, these pinholes represent the area where direct contact between MnO_x and FTO can occur. In addition, we measured the dark current for the $BiVO_4$ samples with different thicknesses of MnO_x in 0.1 M KPi electrolyte. Indeed, the dark current increases for samples with MnO_x films thicker than 4 nm (Fig. 4b), confirming the presence of MnO_x/FTO contact. These observations, therefore, suggest that a shunting effect is the reason behind the decreasing photocurrent for thicker MnO_x films.

The presence of the pinholes, and therefore the shunting pathways, is further confirmed with additional microscopy measurements. The scanning helium ion microscopy top view image of the $BiVO_4$ film shows that it is not fully compact, *i.e.*, some parts of the FTO substrate are not covered (Fig. 5). Fig. 6 shows the scanning transmission electron microscopy (STEM) cross-section image of a $BiVO_4$ sample with 10 nm-thick MnO_x layers. The EDX-STEM mapping (Fig. 6b–f) shows the pinholes on $BiVO_4$ quite clearly. From the composite map (Fig. 6f), the areas in which MnO_x is in direct contact with FTO are marked with the red arrows.

We can now summarize our findings on the role of MnO_x films on $BiVO_4$ and the correlation with the observed photocurrent trend. The deposition of MnO_x co-catalysts on $BiVO_4$ films with increasing MnO_x thickness results in additional band bending at the interface. This leads to lower surface majority
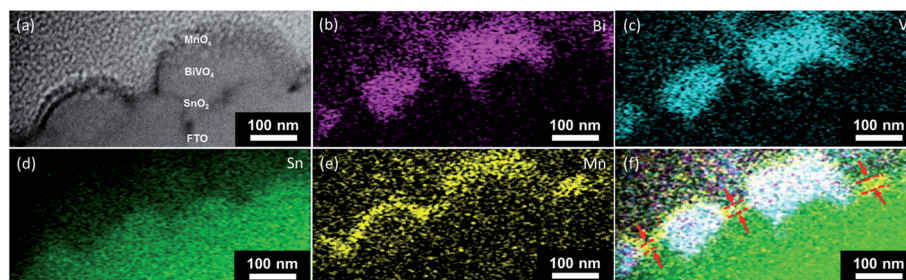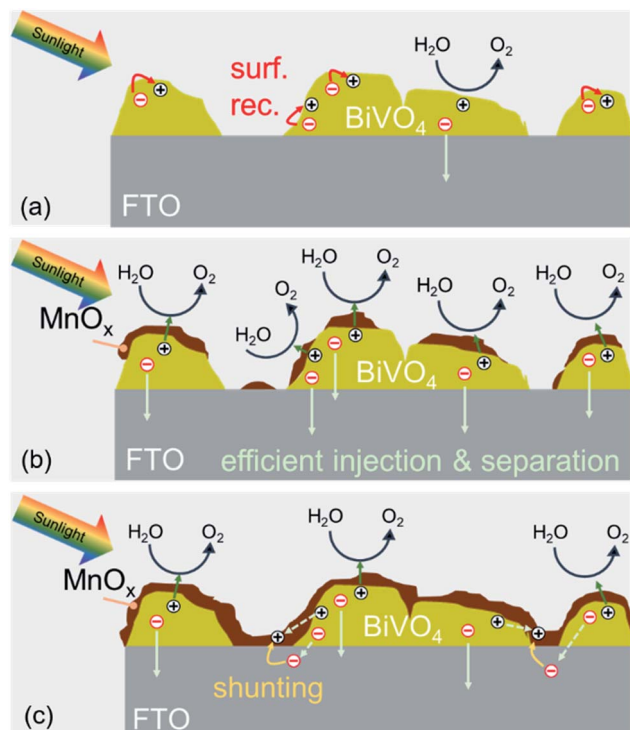

Fig. 6 (a) A cross-section view of the morphology of the $BiVO_4$ films coated with MnO_x. Elemental distribution (net counts, individual intensity scaling) of (b) Bi, (c) V, (d) Sn, (e) Mn, and (f) composite signals as obtained by energy dispersive X-ray spectrometry for MnO_x modified $BiVO_4$.

Scheme 2 (a) In bare $BiVO_4$, charge transfer from the surface of $BiVO_4$ is limited by surface recombination (red arrows). (b) When a thin MnO_x film is deposited on the surface of $BiVO_4$ (up to 4 nm), a discontinuous layer is formed. At the interface, the band bending is enhanced, and the surface recombination is suppressed. (c) Depositing a thicker MnO_x film (>4 nm) leads to a full coverage, even at the exposed FTO surface. Direct contact between MnO_x and FTO results in shunting pathways.

carrier concentration, reduced surface recombination, and higher photocurrent. When the films become too thick, they can make direct contact with the underlying FTO. This causes a shunt between the surface of the $BiVO_4$ and the FTO substrate that causes recombination. These two competing effects (illustrated in Scheme 2) explain the photocurrent being maximized for the $BiVO_4$ films with 4 nm MnO_x co-catalysts.

Conclusions

In summary, we have investigated the role of ultra-thin ALD MnO_x co-catalyst layers on $BiVO_4$ photoanodes. Upon the deposition of MnO_x, the PEC performance of $BiVO_4$ is enhanced. The photocurrent reaches its maximum for a MnO_x thickness of 4 nm ($\sim$3-fold improvement as compared to the bare $BiVO_4$); beyond this thickness the photocurrent decreases. We showed that the MnO_x dark catalytic activity and conductivity trends cannot explain this photocurrent trend. IMPS analysis showed that the charge transfer efficiency and surface recombination rate constant follow the same trend with MnO_x thickness as the photocurrent. We found that MnO_x introduces additional band bending (up to $\sim$0.2 eV) at the $BiVO_4/MnO_x$ interface, as shown from the XPS analysis, which reduces surface recombination. However, at the same time, due to the morphological nature of our spray-pyrolysed $BiVO_4$ films,

increasing the MnO_x thickness also increases the possibility of MnO_x filling the pinholes and creating direct contact with the underlying FTO substrate. We showed that this is indeed the case using electrochemical and TEM analysis. This results in shunting, which increases the electron–hole recombination and cancels out the favorable effect of band bending for thicker MnO_x films. Overall, this study sheds light on the main role of MnO_x co-catalysts on $BiVO_4$ and the underlying reason behind the co-catalyst thickness optimization. It is expected that the phenomena observed in our system can be extended to other semiconductors and co-catalysts, especially those with a similar morphology.

Conflicts of interest

There are no conflicts to declare.

Acknowledgements

References

1 M. G. Walter, E. L. Warren, J. R. McKone, S. W. Boettcher, Q. Mi, E. A. Santori and N. S. Lewis, *Chem. Rev.*, 2010, **110**, 6446–6473.

2 A. J. Bard and M. A. Fox, *Acc. Chem. Res.*, 1995, **28**, 141–145.

3 Y. Tachibana, L. Vayssieres and J. R. Durrant, *Nat. Photonics*, 2012, **6**, 511.

4 M. T. M. Koper, *J. Electroanal. Chem.*, 2011, **660**, 254–260.

5 Gurudayal, L. M. Peter, L. H. Wong and F. F. Abdi, *ACS Appl. Mater. Interfaces*, 2017, **9**, 41265–41272.

6 J. A. Seabold and K.-S. Choi, *J. Am. Chem. Soc.*, 2012, **134**, 2186–2192.

7 Y. Ma, S. R. Pendlebury, A. Reynal, F. Le Formal and J. R. Durrant, *Chem. Sci.*, 2014, **5**, 2964–2973.

8 A. Song, P. Plate, A. Chemseddine, F. Wang, F. F. Abdi, M. Wollgarten, R. van de Krol and S. P. Berglund, *J. Mater. Chem. A*, 2019, **7**, 9183–9194.

9 Y. Park, K. J. McDonald and K.-S. Choi, *Chem. Soc. Rev.*, 2013, **42**, 2321–2337.

10 T. W. Kim and K.-S. Choi, *Science*, 2014, **343**, 990–994.

11 A. Ghosh, N. Kumari and A. Bhattacharjee, *Pramana*, 2015, **84**, 621–635.

12 L. Trotochaud, S. L. Young, J. K. Ranney and S. W. Boettcher, *J. Am. Chem. Soc.*, 2014, **136**, 6744–6753.

13 J. Qiu, H. Hajibabaei, M. R. Nellist, F. A. L. Laskowski, S. Z. Oener, T. W. Hamann and S. W. Boettcher, *ACS Energy Lett.*, 2018, **3**, 961–969.

This journal is © The Royal Society of Chemistry 2020

J. Mater. Chem. A, 2020, **8**, 5508–5516 | **5515**

14 D. K. Zhong, S. Choi and D. R. Gamelin, *J. Am. Chem. Soc.*, 2011, **133**, 18370–18377.

15 M. Kölbach, S. Fiechter, R. van de Krol and P. Bogdanoff, *Catal. Today*, 2017, **290**, 2–9.

16 T. Higashi, H. Nishiyama, Y. Suzuki, Y. Sasaki, T. Hisatomi, M. Katayama, T. Minegishi, K. Seki, T. Yamada and K. Domen, *Angew. Chem., Int. Ed.*, 2019, **58**, 2300–2304.

17 M. Barroso, C. A. Mesa, S. R. Pendlebury, A. J. Cowan, T. Hisatomi, K. Sivula, M. Gratzel, D. R. Klug and J. R. Durrant, *Proc. Natl. Acad. Sci. U. S. A.*, 2012, **109**, 15640–15645.

18 Y.-R. Hong, Z. Liu, S. F. B. S. A. Al-Bukhari, C. J. J. Lee, D. L. Yung, D. Chi and T. S. A. Hor, *Chem. Commun.*, 2011, **47**, 10653–10655.

19 C. Y. Cummings, F. Marken, L. M. Peter, A. A. Tahir and K. G. U. Wijayantha, *Chem. Commun.*, 2012, **48**, 2027–2029.

20 P. S. Bassi, R. P. Antony, P. P. Boix, Y. Fang, J. Barber and L. H. Wong, *Nano Energy*, 2016, **22**, 310–318.

21 J. A. Seabold and K.-S. Choi, *Chem. Mater.*, 2011, **23**, 1105–1112.

22 M. Higashi, K. Domen and R. Abe, *J. Am. Chem. Soc.*, 2012, **134**, 6968–6971.

23 F. F. Abdi, L. Han, A. H. M. Smets, M. Zeman, B. Dam and R. van de Krol, *Nat. Commun.*, 2013, **4**, 2195.

24 H. Ye, H. S. Park and A. J. Bard, *J. Phys. Chem. C*, 2011, **115**, 12464–12470.

25 J. Deng, M. R. Nellist, M. B. Stevens, C. Dette, Y. Wang and S. W. Boettcher, *Nano Lett.*, 2017, **17**, 6922–6926.

26 M. Kim, B. Lee, H. Ju, J. Y. Kim, J. Kim and S. W. Lee, *Adv. Mater.*, 2019, **31**, 1903316.

27 S. D. Tilley, M. Schreier, J. Azevedo, M. Stefik and M. Graetzel, *Adv. Funct. Mater.*, 2014, **24**, 303–311.

28 F. F. Abdi and R. van de Krol, *J. Phys. Chem. C*, 2012, **116**, 9398–9404.

29 M. Chen, Y. Liu, C. Li, A. Li, X. Chang, W. Liu, Y. Sun, T. Wang and J. Gong, *Energy Environ. Sci.*, 2018, **11**, 2025–2034.

30 D. R. Gamelin, *Nat. Chem.*, 2012, **4**, 965–967.

31 Y. Ma, A. Kafizas, S. R. Pendlebury, F. Le Formal and J. R. Durrant, *Adv. Funct. Mater.*, 2016, **26**, 4951–4960.

32 C. Zachäus, F. F. Abdi, L. M. Peter and R. van de Krol, *Chem. Sci.*, 2017, **8**, 3712–3719.

33 M. R. Nellist, J. Qiu, F. A. L. Laskowski, F. M. Toma and S. W. Boettcher, *ACS Energy Lett.*, 2018, **3**, 2286–2291.

34 L. Han, F. F. Abdi, R. van de Krol, R. Liu, Z. Huang, H.-J. Lewerenz, B. Dam, M. Zeman and A. H. M. Smets, *ChemSusChem*, 2014, **7**, 2832–2838.

35 J.-W. Jang, D. Friedrich, S. Müller, M. Lamers, H. Hempel, S. Lardhi, Z. Cao, M. Harb, L. Cavallo, R. Heller, R. Eichberger, R. van de Krol and F. F. Abdi, *Adv. Energy Mater.*, 2017, **7**, 1701536–1701546.

36 F. F. Abdi and S. P. Berglund, *J. Phys. D: Appl. Phys.*, 2017, **50**, 193002–1930023.

37 I. Y. Ahmet, Y. Ma, J.-W. Jang, T. Henschel, B. Stannowski, T. Lopes, A. Vilanova, A. Mendes, F. F. Abdi and R. van de Krol, *Sustainable Energy Fuels*, 2019, **3**, 2366–2379.

38 X. Du, T. Zhao, Z. Xiu, Z. Yang, Z. Xing, Z. Li, S. Yang and W. Zhou, *J. Hazard. Mater.*, 2019, **377**, 330–340.

39 N. C. Strandwitz, D. J. Comstock, R. L. Grimm, A. C. Nichols-Nielander, J. Elam and N. S. Lewis, *J. Phys. Chem. C*, 2013, **117**, 4931–4936.

40 M. Lamers, W. Li, M. Favaro, D. E. Starr, D. Friedrich, S. Lardhi, L. Cavallo, M. Harb, R. van de Krol, L. H. Wong and F. F. Abdi, *Chem. Mater.*, 2018, **30**, 8630–8638.

41 M. Lamers, S. Fiechter, D. Friedrich, F. F. Abdi and R. van de Krol, *J. Mater. Chem. A*, 2018, **6**, 18694–18700.

42 F. F. Abdi and R. van de Krol, *J. Phys. Chem. C*, 2012, **116**, 9398–9404.

43 Y. Liang, T. Tsubota, L. P. A. Mooij and R. van de Krol, *J. Phys. Chem. C*, 2011, **115**, 17594–17598.

44 A. C. Bronneberg, C. Höhn and R. van de Krol, *J. Phys. Chem. C*, 2017, **121**, 5531–5538.

45 E. Langereis, S. B. S. Heil, H. C. M. Knoops, W. Keuning, M. C. M. van de Sanden and W. M. M. Kessels, *In situ* spectroscopic ellipsometry as a versatile tool for studying atomic layer deposition, *J. Phys. D: Appl. Phys.*, 2009, **42**, 073001–073019.

46 R. van de Krol and M. Grätzel, *Photoelectrochemical Hydrogen Production*, Springer, 2012.

47 L. M. Peter, E. A. Ponomarev and D. J. Fermín, *J. Electroanal. Chem.*, 1997, **427**, 79–96.

48 M. Favaro, R. Uecker, S. Nappini, I. Píš, E. Magnano, H. Bluhm, R. van de Krol and D. E. Starr, *J. Phys. Chem. C*, 2019, **123**, 8347–8359.

49 W. W. Gärtner, *Phys. Rev.*, 1959, **116**, 84–87.

50 D. Eisenberg, H. S. Ahn and A. J. Bard, *J. Am. Chem. Soc.*, 2014, **136**, 14011–14014.

51 M. G. Ahmed, I. E. Kretschmer, T. A. Kandiel, A. Y. Ahmed, F. A. Rashwan and D. W. Bahnemann, *ACS Appl. Mater. Interfaces*, 2015, **7**, 24053–24062.

52 A. Kafizas, X. Xing, S. Selim, C. A. Mesa, Y. Ma, C. Burgess, M. A. McLachlan and J. R. Durrant, *Catal. Today*, 2019, **321–322**, 59–66.

53 T. Moehl, W. Cui, R. Wick-Joliat and S. D. Tilley, *Sustainable Energy Fuels*, 2019, **3**, 2067–2075.

5516 | *J. Mater. Chem. A*, 2020, **8**, 5508–5516

This journal is © The Royal Society of Chemistry 2020